Volume 1 | Number 1 | Jan 2013 | Pages 1–100

Journal of
Materials Chemistry A

Materials for energy and sustainability
www.rsc.org/materialsA

Li⁺

ROYAL SOCIETY
OF CHEMISTRY

ROYAL SOCIETY
OF CHEMISTRY

www.rsc.org/materialsA

Journal of Materials Chemistry A

ARTICLE

Ultrathin Single-Crystalline Vanadium Pentoxide Nanoribbons Constructed 3D Networks for Superior Energy Storage

Liujun Cao,[a,b] Jixin Zhu,[c] Yanhong Li,[d] Peng Xiao,[d] Yunhuai Zhang,[a] Shengtao Zhang*[a], Shubin Yang*[b,e]

A new 3D V_2O_5@PPy network built from numerous ultrathin, flexible and single-crystalline nanoribbons was successfully fabricated by a combined hydrothermal, freeze-drying and nanocasting process. Such unique network can not only provide high surface area for enhancement of the electrolyte/electrode interactions, and reduce the diffusion length of ions, but also efficiently maintain the high electrical conductivity. As a result, this network exhibits high capacitance, excellent rate capability and good charge-discharge stability for energy storage. Asymmetric supercapacitor based on 3D V_2O_5@PPy network as cathode material further delivers high energy density and high power density. We expect that our approach presents an efficient approach to design and produce various 3D architectures built from nanoribbons or nanosheets for energy storage and other applications.

1 Introduction

Supercapacitors, also called electrochemical capacitors or ultracapacitors, have been regarded as promising energy storage devices due to their high power density, long lifespan and low cost,[1-3] as well as wide applications such as in emergency power supplies and electric vehicles. However, the energy density of conventional supercapacitors is commonly less than 10 Wh kg^{-1}, much lower than those of batteries and fuel cells, hampering their practical applications. It is well-known that the energy density (E) of a supercapacitor is governed by its capacitance (C) and voltage (V) according to the equation of $E=1/2\ CV^2$. Thus, increasing the device capacitance with novel electrode materials becomes an efficient strategy to improve the energy density of supercapacitors. In this regard, many pseudocapacitive transition-metal oxides (RuO_2,[4] MnO_2,[5] V_2O_5,[6] Co_3O_4,[7]) and conductive polymers[8,11] based on faradic redox-based reactions have been investigated, owing to their higher capacitances than those of electrochemical double-layer capacitive carbon materials. Alternatively, increasing the cell voltage becomes another efficient strategy to improve the energy density of supercapacitors, which has been realized by using organic electrolyte with wide voltage widows.[9,10]

Combined by above two strategies to improve the energy density of supercapacitors, a new concept of asymmetric supercapacitor (ASC) has been recently proposed, which consists of a battery-type Faradic electrode (as energy source) and a capacitor-type electrode (as power source). Thus, ASC not only can make good use of the different voltage windows of two electrodes to maximize the cell voltage, but also can well utilize the high-capacitance electrode materials, resulting in the significant enhancement of energy density.[23,24,30] For instance, transition metal oxides (e.g., MnO_2) and activated carbon have been used as cathode and anode materials, respectively, to fabricate ASC with cell voltages of 2.0 V in aqueous electrolytes. High energy densities of ~12 Wh kg^{-1} was achieved.[31] Unfortunately, the poor conductivity of metal oxide electrodes commonly results in the compromises of power density.[2,12,19] Moreover, the design and fabrication of new electrode materials and appropriate frameworks for asymmetric supercapacitors are still in the infancy.

Herein, we demonstrate a simple approach to fabricate novel three-dimensional (3D) networks built from numerous vanadium penoxides (V_2O_5) nanoribbons by a combined hydrothermal and freeze-drying process. The building blocks of V_2O_5 nanoribbons possess large aspect ratios, ultrathin feature (~2 nm thickness), good flexibility and single-crystalline structure. Moreover, the as-prepared 3D V_2O_5 networks can be facilely encapsulated by conductive polypyrrole (PP$_y$) polymer with an aid of available nanocasting technology (As illustrated in Figure S1). Such unique 3D V_2O_5@PP$_y$ networks (1) provide numerous channels for the access of electrolyte, facilitating the easy diffusion of ions in the electrode, (2) maintain high electrical conductivity of the overall electrode, and (3)

maximize the active material utilization based on redox-reactions. As a consequence, a high capacitance of 502 F g^{-1} with 74% capacitance retention after 10,000 cycles in 1 M Na_2SO_4 aqueous solution is achieved, as 3D $V_2O_5@PP_y$ network is used as the electrode material in a symmetric supercapacitor, very close to the theoretical psedocapacitance value of V_2O_5 (530 F g^{-1}). More importantly, this hybrid network is a promising cathode material for constructing a new asymmetric supercapacitor with 3D reduced graphene oxide foam as anode material. This unique asymmetric supercapacitor exhibits both high energy density of 21.0 Wh kg^{-1} and high power density of 21.5 kW kg^{-1}, as well as good cycle performance.

2 Experimental

2.1 Preparation of 3D pure V_2O_5 networks: In a typical fabrication process, 0.2 mmol V_2O_5 powder, 10 mL 30% H_2O_2 and 70 mL H_2O were mixed to afford a clear solution. The mixture was then transferred and sealed into 100 mL Teflon autoclave. The autoclave was then maintained at 190 ^{o}C for 48 hours to generate red-orange V_2O_5 ribbon gelatin (Figure S1c). Subsequently, the as-prepared gelatin was froze by liquid nitrogen and then dried by a freeze-dry process in order to preserve the high surface area during removal of the residual water. After freeze-dry for 48 hours, the orange-yellow like monolithic gel was produced (Figure S1d).

2.2 Preparation of 3D $V_2O_5@PP_y$ networks: Firstly, PPy solutions were prepared as follows: 0.416 g p-toluenesulfonic acid (p-TSA) was mixed with 30 mL of anhydrous ethanol. After vigorous stirring for 30 minutes, 0.1 mL pyrrole monomer was added into above solution (pyrrole concentration: ~0.048 M) and stirred for another 10 minutes to generate a uniform mixture solution (denoted as solution C). Meanwhile, 0.12 g ammonium persulfate (APS) was dissolved into 20 mL of deionized water under stirring to form a mixture solution (denoted as solution D). The molar ratio of pyrrole monomer to APS was fixed to ~2.747. For 3D $V_2O_5@PP_y$ network synthesis, 30 mg of as-prepared pure 3D V_2O_5 network material was firstly placed in a clean petri dish, and then appropriate volume of solution C (such as 0.3, 0.6, 0.9, 1.2 and 2.4 mL) was dropped into the sample, after 2 minutes, solution D was dropped in the same way (0.3, 0.6, 0.9, 1.2 and 2.4 mL). The samples were subsequently left in the dark environment for 24 hours. Finally, the colour of samples was changed from orange-yellow to dark-green (Figure S1e). We measured the yield of PPy in the reaction by obtaining the final weight of PPy hydrogel at the same recipe without the pure 3D V_2O_5 nanoribbons added (after washing excessive monomers, acids and dried). With the yield value, we calculated the percent of V_2O_5 in the composite between 60 wt% and 95 wt%.

2.3 Fabricating electrodes for symmetric supercapacitors and asymmetric supercapacitors: The symmetric supercapacitors electrodes were prepared by making slurry of 70 wt % active materials, 20 wt % acetylene black, and 10 wt% polytetrafluoroethylene (PTFE; 60 wt% dispersion in water) in

ethanol. The obtained slurry was then coated onto 1.5×1 cm^2 graphite papers within an area of 1×1 cm^2, which were then dried in vacuum at 60 °C for 12 h to remove the solvent. The asymmetric supercapacitors positive electrode was prepared by the same method mentioned above; the negative electrode was prepared by making slurry of 80 wt% 3D reduced graphene oxide, 10 wt% acetylene black, and 10 wt% polytetrafluoroethylene (PTFE; 60 wt% dispersion in water) in ethanol and coated onto 1.5×1 cm^2 graphite papers within an area of 1×1 cm^2, which were then dried in vacuum at 60 °C for 12 h. To fabricate an asymmetric supercapacitor, the loading mass ratio of active material (3D $V_2O_5@PP_y$ network material or 3D reduced graphene oxide foam[21,22]) was estimated to be ~0.33-0.39 according the specific capacitance of 3D $V_2O_5@PP_y$ network material and 3D reduced graphene oxide foam. A 1 M neutral aqueous Na_2SO_4 was used as electrolyte, two piece of nickel foils were connected to the back of graphite papers for the current collectors.

2.4 Electrochemical Measurements: The electrochemical performances of the symmetric supercapacitors device were evaluated via cyclic voltammetry (CV) measurements over a range of scan rates of 5-100 mV s^{-1} in symmetric electrochemical cells with 1 M Na_2SO_4 aqueous electrolyte between 0 and 1.0 V. The galvanostatic charge/discharge measurements were carried out at various current densities from 0.25 A g^{-1} to 10 A g^{-1} over the potential range from 0 to 1.0 V in 1 M Na_2SO_4 aqueous solution using auto-lab equipment (PGSTAT302N). The asymmetric supercapacitor device was evaluated using CV and galvanostatic charge/discharge measurements under the voltage between 0 and 1.8 V. The specific capacitance of the symmetric and asymmetric supercapacitors electrodes were estimated from the galvanostatic discharge curves according to the equation: $C_{single} = 4I \cdot t/m \cdot V$, where m is the total mass of the two electrodes, I is constant discharging current, V is voltage window and t is the discharging time. Electrochemical impedance spectroscopy (EIS) measurements were carried out over the frequency range from 100 kHz to 0.01 Hz by applying a sine wave with amplitude of 5.0 mV under auto-lab equipment (PGSTAT302N). The energy density was calculated as: $E = C_{single} \cdot V_{max}^2/8$. The equivalent series resistance (ESR) was estimated by $R_{ESR} = V_{drop}/(2I)$, while the power density is calculated by the equation $P = V_{max}^2/(4mR_{ESR})$. Both energy density and power density were calculated based on the total mass of active material in the electrodes.

2.5 Characterizations: The morphology and microstructure of the samples were systematically investigated by FE-SEM (JEOL 6500), TEM (JEOL 2010), HRTEM (Field Emission JEOL 2100), XPS (PHI Quantera X-ray photoelectron spectrometer with a monochromated Al kα radiation (hν = 1486.6 eV). All XPS spectra were corrected using the C 1s line at 284.6 eV, curve fitting and background substraction were accomplished using XPS peak fit software), and XRD (Rigaku D/Max Ultima II Powder X-ray diffractometer equipped with Cu kα radiation (λ= 0.15406 nm)) measurements. FTIR spectra ere obtained on a Nicolet FTIR Microscope with an MCT/A

detector. Nitrogen adsorption isotherms for calculating the Brunauer-Emmett-Teller (BET) surface area were measured at 77 K with a Quantachrome Autosorb-3B analyzer (USA).

3 Results and discussion

The morphology and microstructure of as-prepared pure 3D V_2O_5 networks were initially investigated by field-emission scanning electron microscopy (FE-SEM) and high-resolution transmission electron microscopy (HRTEM). As presented in Figure 1a, in the case of freeze-drying process, the highly interconnected and porous 3D architecture built from numerous thin and flexible nanoribbons is visible, whereas the compact film with the strong aggregation of the V_2O_5 ribbons is observed for the sample treated by normal drying method (Figure S2).The lateral sizes of these building block ribbons are typically in the ranges of 100-200 nm in width and several tens of micrometers in length. The representative HRTEM images (Figure 1b and 1c) further reveal their single-crystalline structure. As shown in Figure 1c, the crystalline lattices of 0.19 and 0.18 nm are identified, corresponding to the inter-plane spacing of (600) and (020) planes of orthorhombic V_2O_5, respectively. Correspondingly, the well-defined diffraction patterns (inset in Figure 1c) can be generated by fast Fouries transformation (FFT).[13] To gain further insight to the crystal structure of these nanoribbons, we performed X-ray diffraction (XRD) patterns analysis. As presented in Figure 1d, the main diffraction peaks are located at 6.1^o, 12.2^o, 18.3^o, 24.4^o, 30.5^o and 37.1^o, corresponding to (001), (002), (003), (004), (005) and (006) facets of orthorhombic V_2O_5 (JCPDS No. 40-1296), respectively.[13] Cross-sectional atomic force microscopy (AFM) (Figure 1e) was conducted to further investigate the structural features of V_2O_5 nanoribbons. Their typical AFM image and thickness analyses (Figure 1f and 1g) disclose the same nanoribbon morphology as observations from SEM images, with a uniform thickness of ~2 nm.

The morphology and structure of 3D V_2O_5@PPy network are shown in Figure 2a and 2b. In comparison with those of pure 3D V_2O_5 network, the lateral sizes of the building block ribbons are almost the same (100-200 nm in width and several tens of micrometers in length). A typical HRTEM image of 3D V_2O_5@PPy network reveals that there are many nanograins decorated on the ribbons (Figure 2c, marked by red dot line), totally different from the smooth surface of pure V_2O_5 ribbons, where the well-defined crystalline lattices of V_2O_5 are clearly observed (Figure S3). Moreover, this is different from the reported CoO@PP$_y$ nanowires with clear core-shell structure.[12] To further identify the chemical composition of the hybrid ribbons, we conducted scanning transmission electron microscopy (STEM) and elemental mapping analysis. As shown in Figure 2d-2h, vanadium and oxide elements are fully dispersed into the ribbons, as well as carbon and nitrogen elements are strongly presented on the sites of nanograins, indicating that the nanograins onto the surface of V_2O_5 nanoribbons should be PP$_y$.

To further investigate the crystal structure of 3D V_2O_5@PP$_y$ networks, we performed XRD and X-ray photoelectron spectroscopy (XPS) analysis. As presented in Figure S4a in

Supporting Information, there is a main peak at 6.1^o, and three smaller peaks at 12.2^o, 18.3^o and 24.4^o. Although these peak positions are well consistent with those of pure V_2O_5 nanoribbons (Figure 1d), their intensities are weak, possibly ascribed to the decreased content of V_2O_5 in our same-thick testing holder. The XPS analysis of V_2O_5@PP$_y$ networks (Figure S4b-4f) further discloses the presence of V, O, C and N species with the atomic content of 17.1%，42.9%，33.6% and 6.4% in the ribbons, in good agreement with the previous elemental mapping analysis. The characteristic satellites of V^{5+}2p3/2 and 2p1/2 bands are located at the binding energies of 517.5 and 525 eV, respectively, further demonstrated the formation of V_2O_5 in our sample.[13] The high resolution C1s can be fitted into four energy components centered around 284.1, 284.7, 285.3 and 286.3 eV, corresponding to graphitic carbon (peak 1, 2), aliphatic carbon (peak 3) and carbon species in which carbon bonded to nitrogen (peak 4), respectively.[14] Correspondingly, the N1s spectra can be further deconvoluted into to two different signals with binding energies of 400.3 and 401.0 eV, well consistent with those reported for pyrrolic nitrogen (N-5) and quaternary nitrogen (N-Q) in PPy.[15, 16] The Fourier transform infrared spectroscopy (FTIR) spectra further demonstrate the presence of PPy in our network. As shown in Figure S5, it is clearly seen that there is a band at 1556 cm^{-1}, attributed to the fundamental vibration of pyrrole ring; and another band at 1173 cm^{-1}, characteristic of the C-N stretching vibration.[12] The surface area analysis between pure V_2O_5 network and V_2O_5@PP$_y$ network was studied via the Brunauer-Emmett-Teller (BET) method, which reveals the surface area value of 130 and 35 m^2 g^{-1} for pure V_2O_5 and V_2O_5@PP$_y$ network, respectively (Figure S6).

The electrochemical performances of 3D V_2O_5@PP$_y$ network as electrode material for symmetric supercapacitor (Figure 3a) were firstly evaluated by cyclic voltammetry (CV) measurements over scanning rates of 5-100 mV s^{-1} in 1M Na_2SO_4 aqueous electrolyte (Figure S7 (a)). For comparison, the electrochemical properties of pure 3D V_2O_5 network and V_2O_5 particles@PP$_y$ were also tested under the same conditions. As shown in Figure 3b, at a high scanning rate of 100 mV s^{-1}, V_2O_5@PP$_y$ network shows ideally symmetrical rectangular shape with the highest current density among all the investigated materials, representing the best supercapacitor behavior. The absence of redox peaks in all the voltammograms indicates that both V_2O_5@PP$_y$ electrodes are charged and discharged at a pseudoconstant rate over all the voltammetric cycles,[17] even at low potential scanning rates of 5 and 10 mV s^{-1}(Figure S7). To further compare the electrochemical performances of 3D V_2O_5@PP$_y$ network, pure 3D V_2O_5 network and V_2O_5 particles@PP$_y$, we conducted galvanostatic charge-discharge measurements at various current densities from 0.25 A g^{-1} to 10 A g^{-1} (Figure S7 (b) and (c)). Clearly, the charge-discharge curves of 3D V_2O_5@PP$_y$ network show good symmetry and fairly linear slopes between 0 and 1 V at a current density of 0.5 A g^{-1} (based on the total mass of V_2O_5@PP$_y$ on the two electrodes). Meanwhile, the discharging time of the 3D V_2O_5@PP$_y$ network electrode significantly
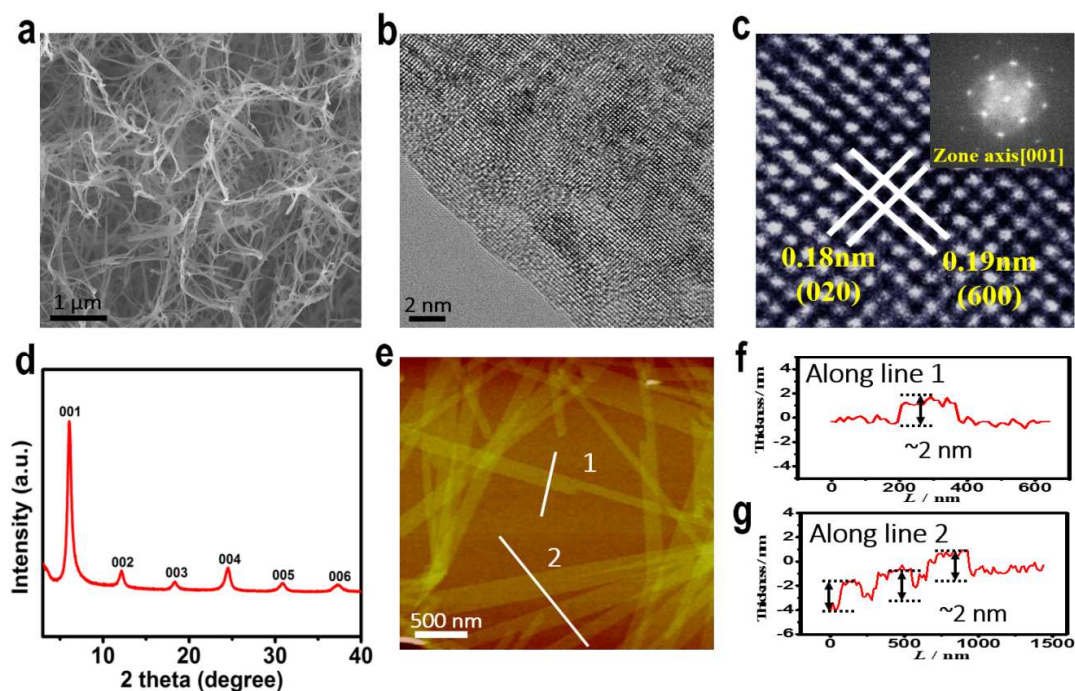
Figure 1. Characterization of pure 3D V_2O_5 networks. (a)Typical SEM image reveals that pure 3D V_2O_5 networks are constructed from numerous nanoribbons. (b-c) HRTEM images with different magnifications and corresponding FFT pattern (insert c) of V_2O_5 ribbons show the single-crystalline structure. (d) XRD patterns of pure 3D V_2O_5 network indicate the orthorhombic V_2O_5 crystal (JCPDS No. 40-1296). (e) Representative atomic force microscopy (AFM) image, and corresponding (f-g) thickness analysis taken around the two white lines (marked as 1 and 2) in (e) reveal uniform thickness of ~2 nm.
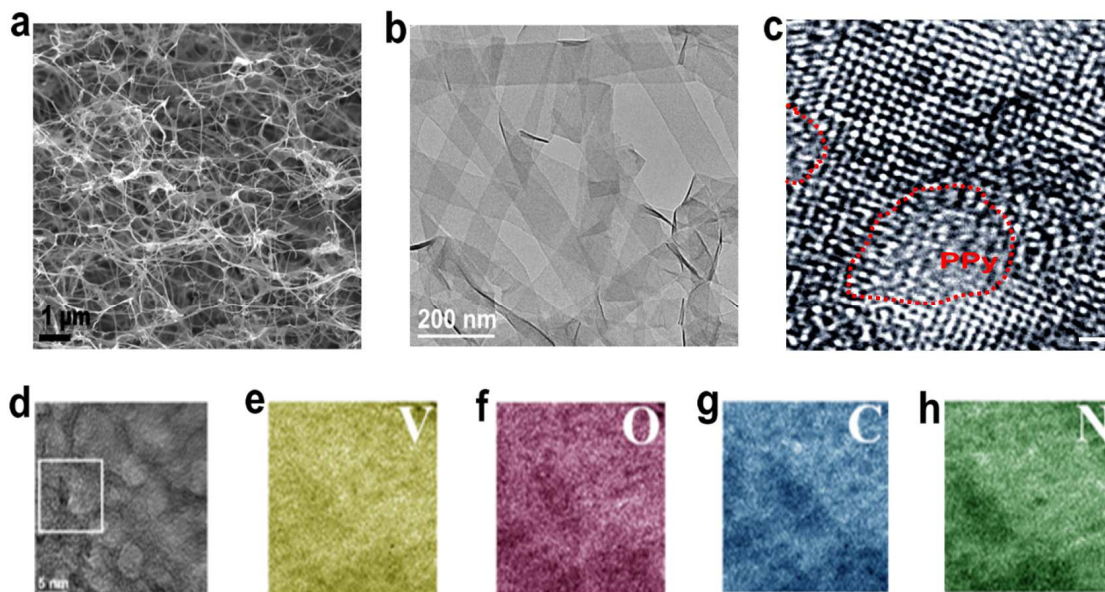

Figure 2. Characterization of 3D V_2O_5 @PPy networks. (a) SEM image of 3D V_2O_5@PPy network shows the networks are constructed from numerous flexible and thin nanoribbons. (b) TEM image discloses that the lateral sizes of V_2O_5@PPy ribbons are typically in the ranges of 100-200 nm in width. (c) HRTEM image of a typical V_2O_5@PPy nanoribbon shows the well-defined V_2O_5 crystalline lattices and PPy nanograins (scale bar, 2 nm). (d) STEM image and its corresponding (e) V, (f) O, (g) C and (h) N element mappings for V_2O_5@PPy hybrid ribbon selected area in (d).

ARTICLE

increases in comparison with the other two electrodes (Figure 3c), suggesting that 3D V_2O_5@PP_y network possesses a higher charge capacitance, well consistent with above CV analysis. The specific capacitances of 3D V_2O_5@PP_y network, pure 3D V_2O_5 network, and V_2O_5 particles@PP_y as a function of the applied current densities are compared in Figure 3d. Remarkably, a high capacitance of 502 F g^{-1} is achieved at current density of 0.25 A g^{-1} in the case of 3D V_2O_5@PP_y network. This value is much higher than those of pure 3D V_2O_5 network (335 F g^{-1}) and V_2O_5 particles@PP_y (84 F g^{-1}), as well as those reported for V_2O_5/carbon composite (295 F g^{-1}),[18] V_2O_5/CNTs (440 F g^{-1}).[19] Moreover, 3D V_2O_5@PP_y network exhibits a good capacitance retention (~74%) compared with pure 3D V_2O_5 network sample (only 52%) after 10,000 cycles at a current density of 2.5 A g^{-1}(Figure 3f). More importantly, at the highest current density of 10 A g^{-1}, the capacitance of the V_2O_5@PP_y network is still stable at 244 F g^{-1}. In contrast, the capacitances of pure V_2O_5 network and V_2O_5 particles@PP_y significantly decease to 130 and 20 F g^{-1}, respectively, similar to those of V_2O_5 nanosheets (90 F g^{-1}, at 10 A g^{-1})[9] and gyroid-structured V_2O_5 network (155 F g^{-1}, at $\sim$10 A g^{-1}) owing to their limited ion incorporation into the electrode material and/or increased resistance for charge transportation during cycling processes.[20] To shed light on this point, we studied the influence of PP_y content in V_2O_5@PP_y networks on the electrochemical properties. As shown in Figure S8, with increasing PP_y content from 5 wt% to 40 wt%, the CV curves of V_2O_5@PP_y networks become distinctly distorted and the specific capacitance largely decreases (Figure S9). This clearly demonstrates that the thick PPy layers hamper the ion incorporation into the electrode materials and reduce the utilization of active materials (V_2O_5 and PPy). Electrochemical impedance spectroscopy (EIS) was further carried out to disclose the kinetic differences between the 3D V_2O_5@PP_y network and pure V_2O_5 network. As shown in Figure 3e, 3D V_2O_5@PP_y network has the smaller semicircle diameter than that of pure 3D V_2O_5 network, indicating that our PPy coating is an efficient strategy to increase the electrical conductivity of pure 3D V_2O_5 network. The detailed kinetic parameters were modeled via the well-known R-C equivalent circuit (Figure S10) and summarized in Table S1. The charge transfer resistance of 3D V_2O_5@PP_y network is only 5.1 Ω, which is lower than those of pure 3D V_2O_5 network electrode (7.4 Ω) and V_2O_5 parcticles@PP_y (8.6 Ω), demonstrating the high electrochemical activity of 3D V_2O_5@PP_y network for energy storage.
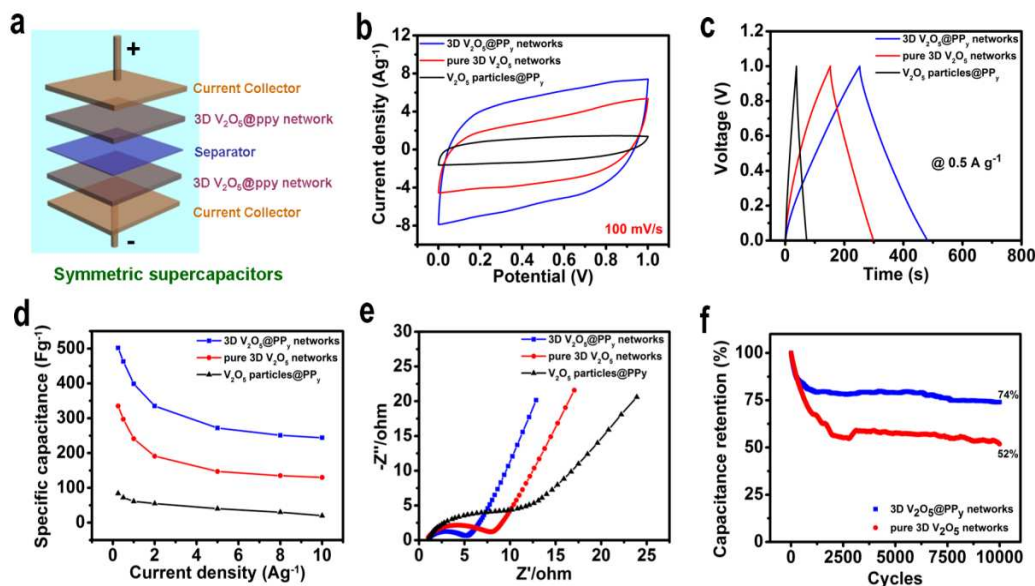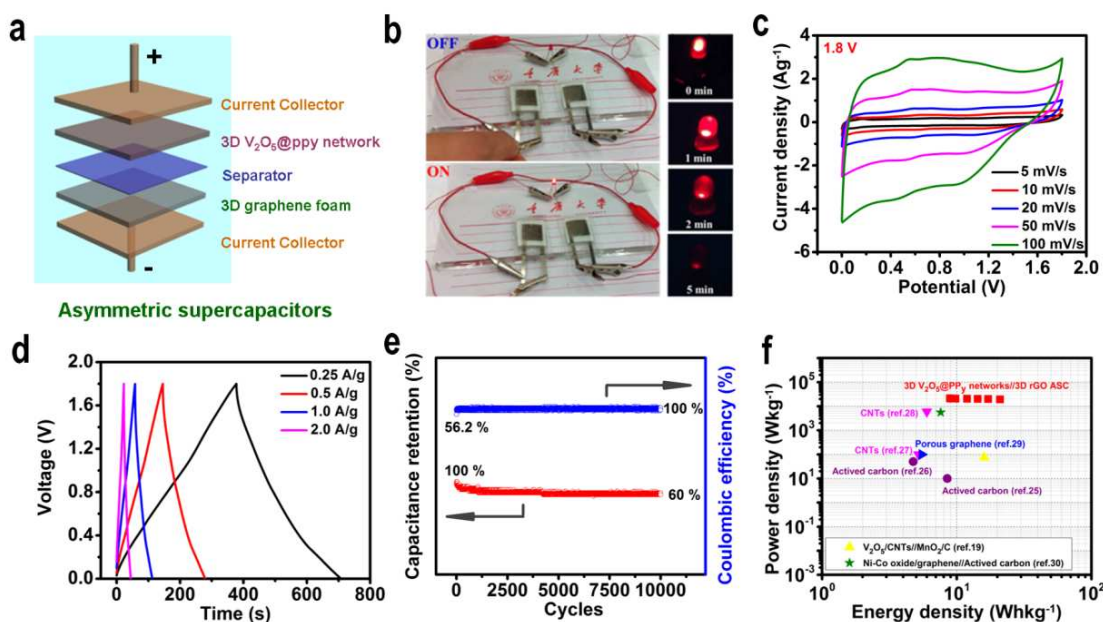

Figure 3. Electrochemical performances of 3D V_2O_5@PPy network in comparison with those of pure 3D V_2O_5 network and V_2O_5 particles@PPy based on symmetric supercapacitors. (a) Schematic of the assembled structure of symmetric supercapacitors by using 3D V_2O_5@PPy network as electrode material. (b) Comparison of their CV curves at a scanning rate of 100 mVs^{-1} . (c) Galvanostatic charge/discharge curves at a current density of 0.5 Ag^{-1} in the range of 0 to 1.0 V in 1M Na_2SO_4 aqueous solution. (d) Specific capacitances calculated from galvanostatic charge/discharge curves with various current densities. (e) Comparable Nyquist plots obtained over the frequency range of 100 kHz to 0.01 Hz. (f) Cycling stabilities of 3D V_2O_5@PPy network and pure V_2O_5 network based on the symmetric supercapacitors.

Journal of Materials Chemistry A

ARTICLE

In addition to the high capacitance, it is known that V_2O_5 possesses wide potential window for energy storage. Hence, our 3D V_2O_5@PP$_y$ network was further chosen as cathode material to construct a new asymmetric supercapacitor with 3D reduced graphene oxide (rGO) foam[21,22] as anode material (Figure 4a). A series of CV measurements were firstly conducted in 1M Na_2SO_4 aqueous electrolyte to estimate the best operating potential. As the operating potential window is below 1.8 V, there are visible redox peaks in the region between 0.2 and 0.8 V, attributed to the energy storage in 3D V_2O_5@PP$_y$ network. While the operating potential is extended to 2.0 V, a distinct peak appears at the end of CV, ascribed to the evolution of oxygen. Correspondingly, the charge-discharge curve is also no longer symmetric indicating non-capacitive behavior (Figure S11). Thus, the potential window of 1.8 V was chosen to study

the electrochemical performances of our asymmetric supercapacitor (Figure 4c and 4d). The galvanostatic charge/discharge analysis (Figure 4d and Figure S12-S13) reveals that our asymmetric supercapacitor exhibits a high specific capacitance of 186 F g^{-1} at a current density of 0.25 A g^{-1}, which is even higher than those recently reported for activated microwave expanded graphite oxide (a-MEGO)-MnO_2//aMEGO (175 F g^{-1} at 0.25 A g^{-1}),[23] and $Ni(OH)_2$/ultrathin-graphite foam (UGF)//a-MEGO (119 F g^{-1} at 1 A g^{-1}) at a higher current density of 1 A g^{-1} (127 F g^{-1}).[24] Furthermore, the capacitance of our asymmetric supercapacitor is still ∼60% of the first capacitance after 10,000 cycles at a current density of 2 A g^{-1} (Figure 4e), representing a good stability for asymmetric pseudocapacitors.

Figure 4. Electrochemical performances of 3D V_2O_5@PPy network based on asymmetric supercapacitors. (a) Schematic of the assembled structure of asymmetric supercapacitors by using 3D V_2O_5@PPy network as positive electrode material and 3D reduced graphene oxide foam as negative electrode material. (b) Photograph of two asymmetric supercapacitor cells in series lighted up one red LED indicator (2 V, 20 mA). (c) CV curves measured at various scanning rates within a potential window of 1.8 V in 1M Na_2SO_4 solution. (d) Galvanostatic charge-discharge curves at different current densities (0.25~2 Ag^{-1}). (e) Cycling stability and coulombic efficiency of the asymmetric supercapacitor. (f) Ragone plots of above asymmetric supercapacitor, in comparison with others reported in literatures.

The energy (E) and power densities (P) of our 3D V_2O_5@PPy networks//3D rGO asymmetric supercapacitor were calculated from galvanostatic discharge curves (based on the total mass of

active material in the electrodes) and plotted on the Ragone diagram shown in Figure 4f. Clearly, a maximum gravimetric energy density of 21.0 Wh kg^{-1} (at a power density of 19.3 kW

kg^{-1}) and maximum power density of 21.5 kW kg^{-1} is achieved for our asymmetric supercapacitor. This value is much higher than those of symmetrical supercapacitors based on activated carbons,[25,26] carbon nanotubes (CNTs)[27,28] and porous graphene (<10 Wh kg^{-1}),[29] as well as the most reported asymmetric supercapacitors in aqueous electrolyte solutions such as V$_2$O$_5$/CNTs//MnO$_2$/C (16 Wh kg^{-1} at power density of 75 W kg^{-1})[19] and Ni-Co oxide/graphene//AC (7.6 Wh kg^{-1} at power density of 5.6 kW kg^{-1})[30]. As a proof of the practical application, we assembled two 3D V$_2$O$_5$@PPy network//3D rGO asymmetric supercapacitors in series. It is clear that our device can power one red round light-emitting diode (LED) (2.0 V, 20mA) indicator after charging for 100 s. Moreover, the red LED can keep very bright for more than 2 min and effective enough for indication for 5 min in a dark environment (as shown in Figure 4b). We believe that the electrochemical performances of our asymmetric supercapacitor can be further improved as increasing the active materials to a commercial supercapacitor level.

Conclusions

In summary, a new 3D network built from V$_2$O$_5$@PP$_y$ nanoribbons with thin nature was successfully fabricated via a combined hydrothermal and freeze-drying approach and subsequent nanocasting process. Such unique 3D V$_2$O$_5$@PP$_y$ network not only can provide the high surface area for enhancement of the electrolyte/electrode interaction, but also can reduce the diffusion length of ions. Moreover, the PPy coating can efficiently maintain the high electrical conductivity of the overall electrode. These lead to the excellent electrochemical performances for energy storage including the high specific capacitance, excellent rate capability and good charge-discharge stability. Asymmetric supercapacitor based on 3D V$_2$O$_5$@PP$_y$ network as cathode material further delivers high energy density and high power density. Our work presents an efficient approach to design and produce various 3D architectures built from nanoribbons or nanosheets for energy storage devices and other applications.

Notes and references

^{a}School of Chemistry and Chemical Engineering, Chongqing University, Chongqing, 400044, China. Email: stzhang@cqu.edu.cn

^{b}Department of Mechanical Engineering & Materials Science, Rice University, Houston, Texas 77005, USA

^{c}TUM CREATE, 1 CREATE Way, #10-02 CREATE Tower, 138602, Singapore

^{d}School of Physics, Chongqing University, Chongqing, 400044, China

^{e}School of Materials Science and Engineering, Beihang University, Beijing, 100191, China. Email: yangshubin@buaa.educn

Author Contributions
L.C. and J.Z. contributed equally to this work.

1 J. R. Miller and P. Simon, *Science*, 2008, **321**, 651.
2 P. Simon and Y. Gogotsi, *Nat Mater*, 2008, **7**, 845.
3 Y. Gogotsi and P. Simon, *Science*, 2011, **334**, 917.
4 C. C. Hu, K. H. Chang, M. C. Lin and Y. T. Wu, *Nano Lett*, 2006, **6**, 2690.
5 R. N. Reddy and R. G. Reddy, *J Power Sources*, 2003, **124**, 330.
6 H. Y. Lee and J. B. Goodenough, *J Solid State Chem*, 1999, **148**, 81.
7 H. J. Kim and S. G. Park, *Electrochemistry*, 2001, **69**, 848.
8 A. Rudge, J. Davey, I. Raistrick, S. Gottesfeld and J. P. Ferraris, *J Power Sources*, 1994, **47**, 89.
9 X. H. Rui, Z. Y. Lu, Z. Y. Yin, D. H. Sim, N. Xiao, T. M. Lim, H. H. Hng, H. Zhang and Q. Y. Yan, *Small*, 2013, **9**, 716.
10 Z. Chen, V. Augustyn, J. Wen, Y. W. Zhang, M. Q. Shen, B. Dunn and Y. F. Lu, *Adv Mater*, 2011, **23**, 791.
11 G. A. Snook, P. Kao and A. S. Best, *J Power Sources*, 2011, **196**, 1.
12 C. Zhou, Y. W. Zhang, Y. Y. Li and J. P. Liu, *Nano Lett*, 2013, **13**, 2078.
13 J. X. Zhu, L. J. Cao, Y. S. Wu, Y. J. Gong, Z. Liu, H. E. Hoster, Y. H. Zhang, S. T. Zhang, S. B. Yang, Q. Y. Yan, P. M. Ajayan and R. Vajtai, *Nano Lett*, 2013, **13**, 5408.
14 T. S. Olson, S. Pylypenko, P. Atanassov, K. Asazawa, K. Yamada and H. Tanaka, *J Phys Chem C*, 2010, **114**, 5049.
15 D. Hulicova-Jurcakova, M. Seredych, G. Q. Lu and T. J. Bandosz, *Adv Funct Mater*, 2009, **19**, 438.
16 L. F. Chen, X. D. Zhang, H. W. Liang, M. G. Kong, Q. F. Guan, P. Chen, Z. Y. Wu and S. H. Yu, *Acs Nano*, 2012, **6**, 7092.
17 S. D. Perera, B. Patel, N. Nijem, K. Roodenko, O. Seitz, J. P. Ferraris, Y. J. Chabal and K. J. Balkus, *Adv Energy Mater*, 2011, **1**, 936.
18 B. Wang, K. Konstantinov, D. Wexler, H. Liu and G. X. Wang, *Electrochim Acta*, 2009, **54**, 1420.
19 Z. Chen, Y. C. Qin, D. Weng, Q. F. Xiao, Y. T. Peng, X. L. Wang, H. X. Li, F. Wei and Y. F. Lu, *Adv Funct Mater*, 2009, **19**, 3420.
20 D. Wei, M. R. J. Scherer, C. Bower, P. Andrew, T. Ryhanen and U. Steiner, *Nano Lett*, 2012, **12**, 1857.
21 S. B. Yang, Y. J. Gong, Z. Liu, L. Zhan, D. P. Hashim, L. L. Ma, R. Vajtai and P. M. Ajayan, *Nano Lett*, 2013, **13**, 1596.
22 Y. Xu, K. Sheng, C. Li and G. Shi, *Acs Nano*, 2010, **4**, 4324.
23 X. Zhao, L. L. Zhang, S. Murali, M. D. Stoller, Q. H. Zhang, Y. W. Zhu and R. S. Ruoff, *Acs Nano*, 2012, **6**, 5404.
24 J. Y. Ji, L. L. Zhang, H. X. Ji, Y. Li, X. Zhao, X. Bai, X. B. Fan, F. B. Zhang and R. S. Ruoff, *Acs Nano*, 2013, **7**, 6237.
25 D. W. Wang, F. Li, M. Liu, G. Q. Lu and H. M. Cheng, *Angew Chem Int Edit*, 2008, **47**, 373.
26 C. Zheng, L. Qi, M. Yoshio and H. Y. Wang, *J Power Sources*, 2010, **195**, 4406.
27 C. J. Yu, C. Masarapu, J. P. Rong, B. Q. Wei and H. Q. Jiang, *Adv Mater*, 2009, **21**, 4793.
28 M. Kaempgen, C. K. Chan, J. Ma, Y. Cui and G. Gruner, *Nano Lett*, 2009, **9**, 1872.
29 J. Yan, Z. J. Fan, W. Sun, G. Q. Ning, T. Wei, Q. Zhang, R. F. Zhang, L. J. Zhi and F. Wei, *Adv Funct Mater*, 2012, **22**, 2632.

30   H. L. Wang, C. M. B. Holt, Z. Li, X. H. Tan, B. S. Amirkhiz, Z. W. Xu, B. C. Olsen, T. Stephenson and D. Mitlin, *Nano Res*, 2012, **5**, 605.

31   T. Brousse, P. L. Taberna, O. Crosnier, R. Dugas, P. Guillemet, Y. Scudeller, Y. Zhou, F. Favier, D. Belanger and P. Simon, *J Power Sources*, 2007, **173**, 633-641.

TOC figure
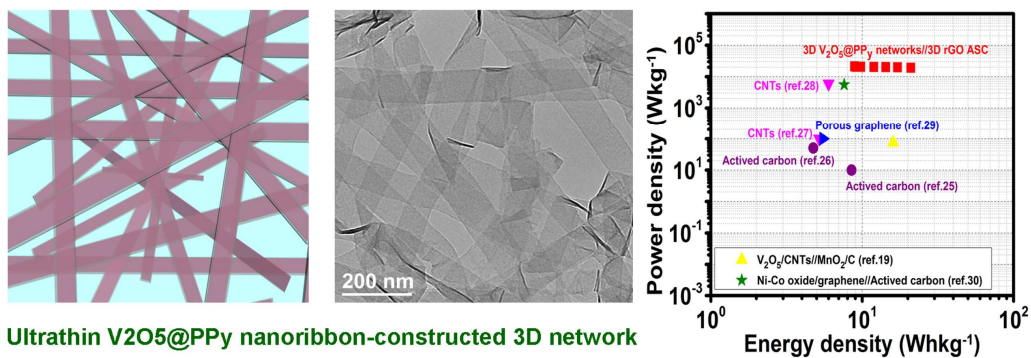
Ultrathin V2O5@PPy nanoribbon-constructed 3D network

A new 3D V$_2$O$_5$@PPy network built from numerous ultrathin, flexible and single-crystalline nanoribbons was successfully fabricated for superior energy storage.